Biomaterials Science

ROYAL SOCIETY OF CHEMISTRY

PAPER

View Article Online
View Journal | View Issue

Cite this: *Biomater. Sci.*, 2025, **13**, 4447

Metabolic click-labeling of interleukin-10 enhances the immunomodulatory potential and wound healing properties of mesenchymal stem cell-derived extracellular nanovesicles†

Hee Gyeong Ko,[a,b] Yun-A Kim,[a,b] Jun Kwon,[a,b] So Won Jeon,[a,b] Jong Sang Yoon,[a,b] Min-Ho Kang,[a,b] Ju-Ro Lee[c,d] and Han Young Kim *[a,b]

Mesenchymal stem cell-derived extracellular nanovesicles (MSC-NVs) exhibit unique biological properties and tissue-regenerative effects comparable to their parent MSCs. However, despite the robust angiogenic and anti-apoptotic effects of MSC-NVs, their immunomodulatory effect is limited due to insufficient translation of anti-inflammatory cytokines from parent MSCs to isolated NVs. Hence, in this study we suggest the incorporation of interleukin (IL)-10, a key anti-inflammatory mediator in the body's immune system, on the surface of MSC-NVs *via* bio-orthogonal click chemistry. Metabolically engineered MSCs were serially extruded to generate azido-displaying MSC-NV-N_3, followed by click chemistry-based conjugation of IL-10. Synthesized MSC-NV/IL-10 exhibited superior abilities for cell proliferation and migration of fibroblast and endothelial cells. MSC-NV/IL-10 markedly attenuated the activity of the pro-inflammatory M1 macrophage and promoted the expression of the anti-inflammatory M2 marker. We also demonstrated that MSC-NV/IL-10 induces the phenotypic transition of dendritic cells (DCs) from mature DCs to immune-tolerogenic DCs. Moreover, RNA sequencing revealed that metabolic engineering does not alter the regenerative potential or immunomodulatory functions of MSCs. In animal studies, MSC-NV/IL-10 treated mice exhibited significantly accelerated wound healing, accompanied by resolution of inflammatory responses in injured skin.

Received 30th November 2024,
Accepted 22nd June 2025

DOI: 10.1039/d4bm01601g

rsc.li/biomaterials-science

Introduction

Stem cell therapy has been applied to various diseases and injuries. The administration of mesenchymal stem cells (MSCs) has emerged as a particularly promising therapeutic strategy in regenerative medicine and tissue engineering, due to their ability to secrete bioactive molecules and paracrine factors.[1,2] However, recent studies have revealed that MSCs exhibit low survival rates in inflammatory and hypoxic environments and do not effectively replace damaged cells at the injection site.[3] To address these limitations, research has focused on MSC-derived exosomes as a potential alternative to direct MSC transplantation. Despite their therapeutic potential, the complex purification process and low production yield of MSC-derived exosomes pose significant challenges for large-scale clinical applications.[4,5] A large number of MSCs are required to produce a sufficient amount of exosomes; however, repeated subculturing is a common underlying cause of MSC senescence.[6] Cellular senescence severely weakens the ability of stem cells to repair and regenerate.[7] To overcome these challenges, MSC-derived extracellular nanovesicles (MSC-NVs) have emerged as an alternative therapeutic agent, exhibiting biological functions comparable to those of parent MSCs or MSC-exosomes.[8,9] Importantly, MSC-NVs contain intracellular components such as proteins, lipids, mRNAs, and microRNAs, which are associated with immune regulation, inflammation reduction, and tissue regeneration.[10] Furthermore, the manufacturing process of MSC-NVs provides higher production efficiency and greater consistency in size and content compared to naturally secreted exosomes.[11,12] As a cell-free therapeutic approach, MSC-NVs do not replicate or mutate, making them more suitable for long-term storage compared to live MSCs. Moreover, MSC-NVs inherently target inflamed or

[a]*Department of Biotechnology, The Catholic University of Korea, Bucheon-si, Gyeonggi-do, Republic of Korea. E-mail: hy0408@catholic.ac.kr; Tel: +82-2-2164-4002*
[b]*Department of Biomedical-Chemical Engineering, The Catholic University of Korea, Bucheon-si, Gyeonggi-do, Republic of Korea*
[c]*Center for Systems Biology, Massachusetts General Hospital Research Institute, Boston, MA, USA*
[d]*Department of Radiology, Massachusetts General Hospital, Harvard Medical School, Boston, MA, USA*

† Electronic supplementary information (ESI) available. See DOI: https://doi.org/10.1039/d4bm01601g

damaged tissues owing to their surface molecules, which interact with receptors on target cells.[13,14] Therefore, MSC-NVs have been recognized as potent therapeutic agents that are capable of clinical-scale production.[15]

Interleukin-10 (IL-10) is a major anti-inflammatory and immunomodulatory cytokine.[16,17] It regulates immune responses, promotes cell proliferation, and supports the extracellular matrix and fibroblast function by binding to their receptors on immune cells. Upon receptor binding, IL-10 activates downstream signaling pathways, such as the JAK-STAT pathway, leading to gene expression changes that suppress inflammation.[18,19] Notably, IL-10 induces M2-type macrophage polarization,[20] which facilitates inflammation reduction, extracellular matrix remodeling, and promoting angiogenic factors.[21,22] Moreover, IL-10 promotes dendritic cell (DC) differentiation into tolerogenic DCs (tolDCs), which exhibit immune-suppressive properties and hold significant potential for autoimmune disease therapy.[23,24] Collectively, IL-10 has been extensively investigated as a therapeutic agent for inflammatory diseases.[25,26] Despite its potent anti-inflammatory properties, IL-10 has a short biological half-life and undergoes rapid degradation, which significantly limits its clinical application.[27] Thus, the development of delivery strategies is crucial for enhancing the therapeutic efficacy of IL-10 at inflamed and injured sites.

Click chemistry is widely applied in biomedical nanomaterials for efficient and selective bioconjugation. Among the various click reactions, bio-orthogonal metabolic labeling has gained particular attention for conjugating therapeutic molecules onto the surface of live cells.[28] Due to its high specificity, stability, and biocompatibility, bio-orthogonal click chemistry has been widely applied to cell engineering.[29,30] The azide-containing glycoprotein labeling agent, *N*-azidoacetyl-D-mannosamine (Ac_4ManNAz), enables the incorporation of azide (N_3) groups onto cell membrane surfaces.[31,32] Interestingly, Ac_4ManNAz-induced cells incorporate azide moieties into the bilayer lipids of extracellular vesicles (EVs).[33] Dibenzocyclooctyne (DBCO) covalently binds to azide groups, forming stable triazoles without requiring catalysts, thereby enabling precise and stable cell surface labeling without altering cellular biochemistry.[34]

Together, in this study, we functionalized the external lipid bilayer of MSC-NVs with IL-10 using bio-orthogonal click chemistry. Metabolically labeled MSCs were serially extruded to generate N_3-displaying MSC-NVs (MSC-NV-N_3) followed by conjugation with DBCO-tagged IL-10, resulting in the MSC-NV/IL-10 complex (Fig. 1). We investigated the pro-angiogenic and anti-apoptotic effects of MSC-NV/IL-10 in fibroblast and endothelial cells. Furthermore, bone marrow-derived macrophages (BMDMs) and bone marrow-derived dendritic cells (BMDCs) were harvested from mice and treated with MSC-NV/IL-10 for evaluation of anti-inflammatory responses. Finally, we evaluated the regenerative and anti-inflammatory effects of MSC-NV/IL-10 in a full-thickness skin wound mouse model. RNA-sequencing (RNA-seq) was performed on MSCs and MSC-N_3 to verify whether metabolic labeling causes significant transcriptional changes in MSCs.

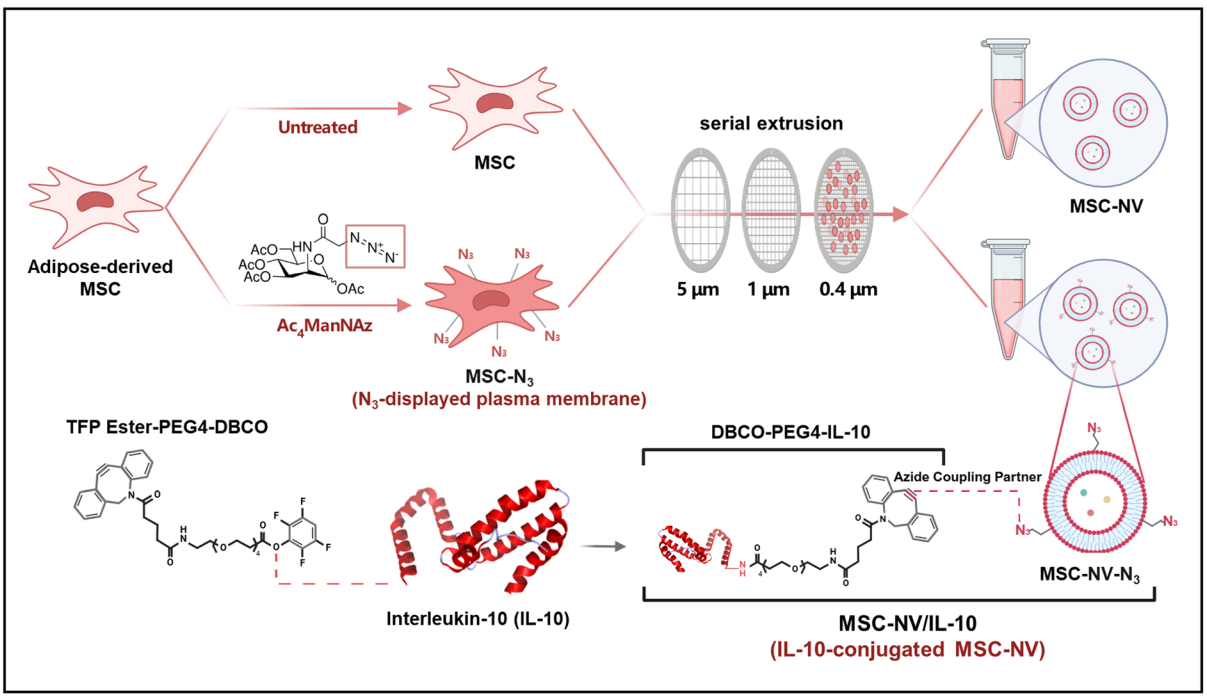

Fig. 1 Schematic illustration showing metabolic glycoengineering of MSCs and fabrication of MSC-NV/IL-10 *via* click chemistry. After metabolic labeling of MSCs with Ac_4ManNAz to introduce azido (N_3) groups on their membrane surfaces, MSC-NV-N_3 was fabricated by serial extrusion. Bio-orthogonal click chemistry-based conjugation of DBCO-tagged IL-10 subsequently yields the MSC-NV/IL-10 complex.

Materials and methods

Cell culture

Human adipose-derived mesenchymal stem cells (MSCs) with passage numbers of 5–7 (Lonza, Switzerland) and L929 murine fibroblasts (Korean Cell Line Bank, Korea) were cultured in DMEM (Gibco, USA) supplemented with 10% (v/v) fetal bovine serum (FBS; Gibco, USA) and 1% (v/v) penicillin/streptomycin (PS; Gibco, USA). BMDMs and BMDCs were isolated from the femurs and tibias of mice and cultured in RPMI 1640 medium (Gibco, USA) containing 10% (v/v) FBS and 1% (v/v) PS. Human umbilical vein endothelial cells (HUVECs; PromoCell, Germany) were cultured in an endothelial cell growth medium (EGM; PromoCell, Germany). All cells were incubated at 37 °C in a humidified atmosphere with 5% CO_2.

Isolation and differentiation of BMDMs and BMDCs

BMDMs and BMDCs were generated from 6 week-old female C57BL/6 mice (Koatech, South Korea). Mouse femur and tibia were isolated, and bone marrow was flushed out using a 25-gauge needle. The isolated bone marrow cells were reconstituted in RPMI 1640 medium, supplemented with 10% (v/v) FBS and 1% (v/v) PS. To induce the differentiation to BMDMs, 10% (v/v) L929-conditioned medium was added. Cells were plated in a 100 mm Petri dish at a concentration of 4×10^5 cells per mL and after 3 days, 10 mL of fresh medium was added. For BMDCs, 20 ng mL^{-1} recombinant murine GM-CSF (R&D Systems, USA) was added to support DC differentiation. Cells were plated in a Petri dish at a concentration of 1×10^6 cells per mL and on day 3, half of the medium was added. BMDMs and BMDCs were collected on day 6 and used for further experiments.

Bio-orthogonal labeling of MSCs

For metabolic labeling of cultured MSCs, cells were seeded onto coverslips placed in a 12-well culture plate at a density of 1×10^4 cells per well and incubated with 50 μM $Ac_4ManNAz$ for 72 hours. Subsequently, the cells were treated with 40 μM DBCO-Cy5 (Sigma, Germany) for 30 minutes at 37 °C. Following the incubation, the cells were washed twice with phosphate-buffered saline (PBS) and fixed with 4% paraformaldehyde solution for 10 minutes in a dark environment. The fixed cells were washed twice with PBS and mounted with a DAPI solution (VWR, USA). The cells were visualized using a fluorescence microscope (Eclipse Ti2, Nikon, Japan) and additionally evaluated using flow cytometry (CytoFlex, Beckman Coulter, USA), and resulting data were analyzed using FlowJo software (BD Biosciences).

Preparation of MSC-NVs and MSC-NV-N_3

Once the MSCs or $Ac_4ManNAz$-treated MSCs (MSC-N_3) reached 90% confluence in 150 mm^2 culture dishes, the cells were harvested using a cell scraper. The cells were washed and resuspended in PBS. To isolate NVs, the collected cells were disrupted by ultrasonication and serially extruded through a series of membrane filters with pore sizes of 5 μm, 1 μm, and 0.4 μm (Avanti Polar Lipids, USA). The cells were extruded ten times through each membrane filter. Following serial extrusion, the NVs were centrifuged at 1000*g* for 10 min to remove nuclei. Fabricated NVs were purified by ultracentrifugation at 27 000*g* for 2 hours. The pellet of NVs was then resuspended in PBS. The fabricated NVs were then stored at −80 °C until needed.

Synthesis of DBCO-IL-10 and preparation of MSC-NV/IL-10

To prepare DBCO-tagged IL-10 (DBCO-IL-10), EZ-Link TFP Ester-PEG4-DBCO (Thermo Scientific, USA) was first diluted in DMSO to obtain a final concentration of 3.5 mM. Then, recombinant murine IL-10 (Sino Biological, China) was incubated with a 100-fold molar excess of TFP Ester-PEG4-DBCO at room temperature for 3 hours. As-synthesized DBCO-IL-10 was purified *via* Zeba spin desalting columns (Thermo Scientific, USA). For the synthesis of MSC-NV/IL-10, MSC-NV-N_3 was mixed with DBCO-IL-10 at a protein-to-protein ratio of 1000 : 1 and incubated overnight at 4 °C for complete conjugation. To remove the unbound DBCO-IL-10, the mixture was centrifuged and washed twice with PBS.

Characterization of NVs

The morphology of MSC-NV-N_3 was analyzed using a cryogenic transmission electron microscope (cryo-TEM). A 3 μL aliquot of the sample solution was applied on a glow discharged holey carbon grid (Quantifoil R1.2/1.3, 200 mesh Cu, USA) under controlled conditions of 15 °C and 100% humidity inside a Vitrobot Mark IV chamber (Thermo Fisher, USA, SNU CMCI). The excess solution on the grid was blotted for 3 s at blotting force level 1, and the grid was plunge frozen in liquid ethane. The cryogenic sample was transferred to a cryo-TEM holder (626 single tilt, USA) while maintaining a temperature of approximately −180 °C. Cryo-TEM imaging was performed using TEM (JEM-2100F, Japan) with a total dose of ~20 $e^- Å^{-2}$. The sizes and zeta potentials of the fabricated MSC-NVs, MSC-NV-N_3, and MSC-NV/IL-10 were measured through dynamic light scattering (DLS; Malvern, USA) after dispersing the particles in PBS. The size and number of synthesized NVs were also determined using ZetaView (Particle Metrix, Germany) for nanoparticle tracking analysis (NTA). To fluorescently label DBCO-IL-10, thiolation was performed using Traut's reagent (Thermo Scientific, USA). DBCO-IL-10 was incubated with a 10-fold molar excess of Traut's reagent at room temperature for 1 hour. Unreacted Traut's reagent was removed using Zeba spin desalting columns (Thermo Scientific, USA). Thiolated DBCO-IL-10 was then labeled with a 20-fold molar excess of Alexa fluor 647 C_2 maleimide (Invitrogen, USA) and incubated overnight at 4 °C for complete conjugation. Excess maleimide was removed *via* Zeba spin desalting columns. The fluorescently labeled DBCO-IL-10 was subsequently conjugated to MSC-NV-N_3 at a protein-to-protein ratio of 1000 : 1 and incubated overnight at 4 °C. Unbound IL-10 was removed by centrifugation and washing with PBS. To determine the cellular uptake of different NVs in HUVECs, 100 μg mL^{-1} NVs were stained with Vybrant DiO solution

(Invitrogen, USA) at 37 °C for 30 minutes. DiO-labeled NVs, conjugated with DBCO-IL-10 or DBCO-Cy5, were then applied on HUVECs and incubated for 6 hours. The cells were subsequently observed using a fluorescence microscope. Fluorescence profiles were obtained using NIS-Elements software (Nikon).

Evaluation of *in vitro* pro-angiogenic and anti-apoptotic effects

The migration and proliferation assays were conducted on L929 cells and HUVECs treated with 40 μg mL^{-1} MSC-NVs, MSC-NV-N_3, or MSC-NV/IL-10. Proliferation was evaluated at 0, 24, and 48 hours after incubation using a CCK-8 assay kit (EZ-Cytox, DoGenBio, Korea). To create a consistent cell-free area for the migration assay, ScarBlock (SPL, Korea) was used. Cells were seeded at a density of 2×10^4 cells per block and the medium was replaced with serum-free medium containing respective treatments. At 0, 24, and 48 hours after treatment with NVs, the cells were washed and stained with DiO for 30 min. The cells were visualized with a fluorescence microscope and the cell-free area was quantified using ImageJ software. To investigate anti-apoptotic effects, HUVECs were treated with different NVs for 24 hours in the presence of 1 mM H_2O_2. For flow cytometric analysis, the cells were double-stained with Annexin V-FITC and propidium iodide (PI) (BioLegend, USA) following the manufacturer's instructions.

Quantitative real-time PCR and RNA sequencing

A quantitative real-time polymerase chain reaction (qRT-PCR) was performed to evaluate the mRNA expression of various genes. Total RNA was extracted from the cells using TRIzol reagent (Thermo Scientific, USA). The concentration of total RNA was determined using a NanoDrop spectrophotometer (Thermo Fisher, USA). A cDNA synthesis kit (Bioneer, Korea) was used to synthesize cDNA from total RNA by following the manufacturer's instructions. Gene expressions were evaluated using a StepOnePlus real-time PCR system (Applied Biosystems, USA) The primers used for qRT-PCR are detailed in Fig. S1.† For RNA sequencing, total RNA from MSCs and Ac_4ManNAz-treated MSCs were isolated. The library was prepared and sequenced on an Illumina platform (Illumina NovaSeq X Plus PE150) through the service provided by Novogene (Singapore).

Assessment of the immunomodulatory effect of NVs in BMDMs and BMDCs

For evaluation of macrophage polarization, BMDMs were incubated in the presence of lipopolysaccharides (LPSs, 100 ng mL^{-1}) and interferon-gamma (IFN-γ, 20 ng mL^{-1}) or in the absence of LPS/IFN-γ for 24 hours. Following the removal of the medium, cells were treated with 40 μg mL^{-1} of different NVs. After 24 hours of treatment, the cells were harvested and stained with FITC-conjugated anti-mouse F4/80, PE-conjugated anti-mouse CD86, or APC-conjugated anti-mouse CD206 antibodies (BioLegend, USA). The stained cells were analyzed using flow cytometry and the resulting data were analyzed using FlowJo software. Additionally, qRT-PCR was carried out to assess gene expressions of IL-1β, TNF-α, IL-6, and Arg-1. To evaluate the expression of costimulatory molecules in BMDCs, 40 μg mL^{-1} of different NVs were co-treated with LPS for 24 hours. Following incubation, the phenotypic characteristics of DCs were analyzed by flow cytometry using FITC-conjugated anti-mouse CD11c, APC-conjugated anti-mouse CD206, PE-conjugated anti-mouse CD86, and APC/Cy7-conjugated anti-mouse CD40 (BioLegend).

Animal wound model

Female C57BL/6 mice (8 weeks) were purchased from Orient Bio (Seongnam, Korea). The mice were randomly allocated into control, MSC-NVs, and MSC-NV/IL-10 groups and then anesthetized using an isoflurane gas. The dorsal hairs of the mice were shaved and sterilized, and a roundthick wound was made on the dorsal skin of the mice using a sterile 6 mm biopsy punch tool. Immediately, 80 μg of MSC-NVs conjugated with 100 ng of IL-10 per treatment were topically applied to the wound every 3 days. Following treatment, the wounds were covered with transparent Tegaderm dressing (3M, USA). On 0, 3, 6, and 9 days of post-wounding, the wounds were photographed and measured.

Histological analysis

On day 6, wound samples from each group were used to analyze the macrophage and dendritic cell polarization of MSC-NV/IL-10 treatment. Mice were euthanized by CO_2 gas asphyxiation and wound tissues were cut off and fixed with 4% paraformaldehyde overnight. The sections were embedded in paraffin and cut into 4 μm sections. For immunohistochemistry (IHC), the sections were blocked with 10% of goat serum for 2 hours. Following blocking, sections were incubated with primary antibodies; FITC-conjugated anti-mouse F4/80, FITC-conjugated anti-mouse CD11c, Alexa 594-conjugated anti-mouse iNOS, Alexa 547-conjugated anti-mouse CD80, and Alexa 647-conjugated anti-mouse CD86 (BioLegend, USA), or Alexa 647-conjugated anti-mouse CD163 antibodies (Thermo Fisher, USA). Finally, the stained sections were counterstained with DAPI. The images were obtained using a fluorescence microscope. For hematoxylin and eosin (H&E) staining, the tissues were embedded in paraffin and cut into 5 μm sections. The sections were deparaffinized, rehydrated, and stained with hematoxylin for nuclear visualization, followed by eosin staining to highlight cytoplasmic and extracellular components. The stained sections were dehydrated and mounted with a permanent mounting solution, and images were obtained using a light microscope.

Statistical analysis

Statistical analysis was performed using GraphPad Prism software. The data are presented as mean ± standard deviation (SD). Values are representative of three or more independent experiments per group. The *p*-values were calculated by one-way or two-way analysis of variance with Tukey's test. Values of $p < 0.05$ were considered statistically significant.

Results

Metabolic glycoengineering of MSCs and fabrication of MSC-NV/IL-10 *via* click chemistry

To introduce azide (N_3) moieties on the cell membrane surface, cultured MSCs were treated with 50 μM Ac_4ManNAz for 3 days. The expression of the azide functional groups on the membranes of Ac_4ManNAz-treated MSCs (MSC-N_3) was verified by incubation with DBCO-Cy5. Fluorescence microscopy observation revealed markedly enhanced Cy5 fluorescence in MSC-N_3 relative to untreated MSCs (Fig. 2A). Fluorescence signals of DBCO-Cy5 were specifically located at the plasma membrane of MSC-N_3, demonstrating the stable expression of azide groups on the cell membrane surface. Flow cytometry histogram and mean fluorescence intensity (MFI) also indicated that the MSC-N_3 exhibited an approximately 2.72-fold increase in MFI for DBCO-Cy5 compared to unmodified MSCs (Fig. 2B). These findings demonstrate the successful expression of N_3 on the membrane surface of MSCs. Cytotoxicity was evaluated by exposing MSCs to various

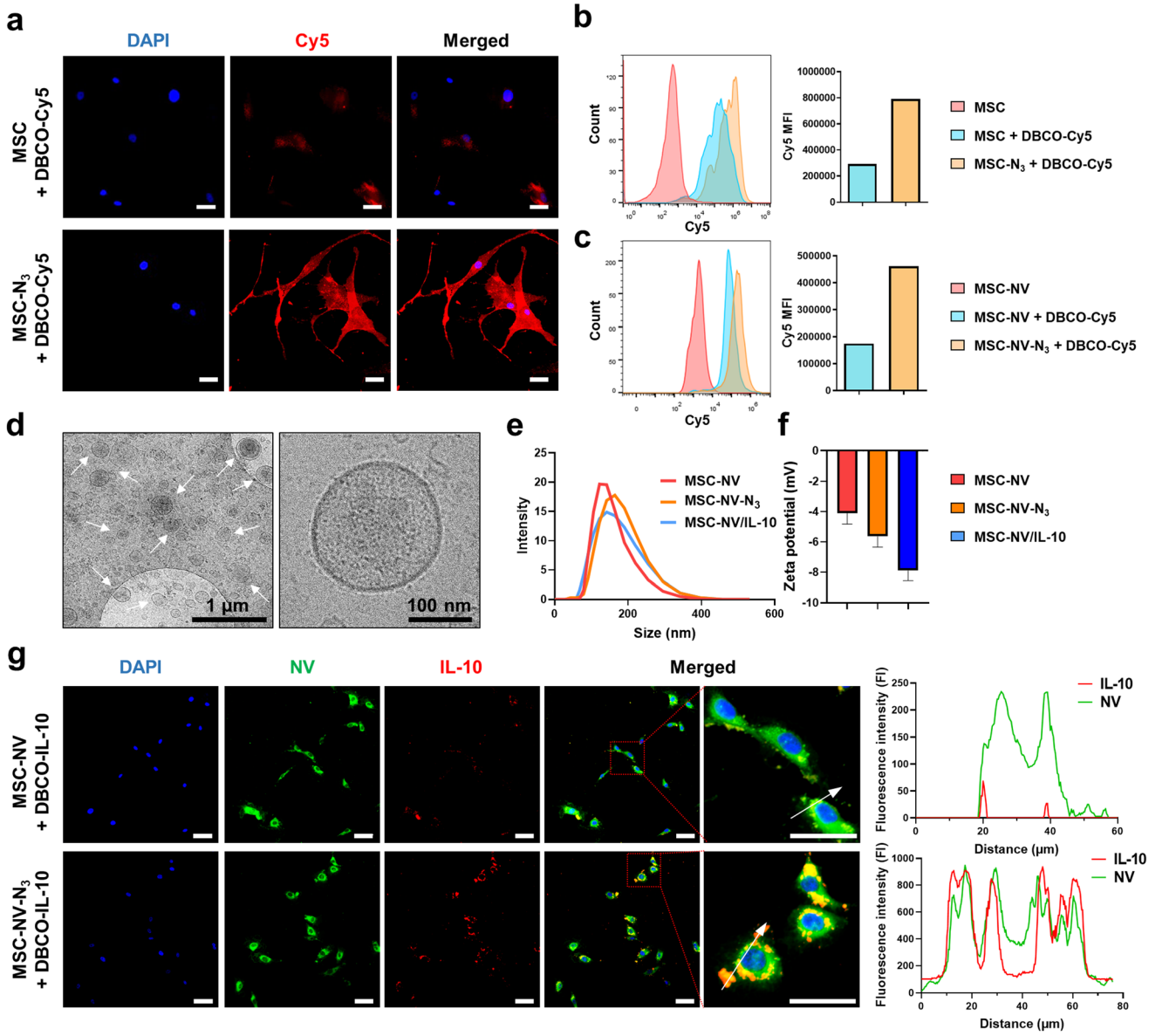

Fig. 2 Ac4ManNAz-induced N3 expression of MSCs and characterization of NVs. (a) Fluorescence microscopy images of MSCs after treatment with Ac4ManNAz (50 μM) for 72 h, followed by incubation of DBCO-Cy5 (red). Cell nuclei were stained with DAPI (blue). Scale bar: 10 μm. (b) Flow cytometric analysis and quantification showing enhanced conjugation of DBCO-Cy5 with MSC-N_3. (c) Flow cytometric analysis and quantification showing enhanced conjugation of DBCO-Cy5 with MSC-NV-N_3. (d) Cryo-TEM images of isolated MSC-NV-N_3. (e) Size distribution and (f) zeta potential of MSC-NVs, MSC-NV-N_3, and MSC-NV/IL-10. (g) Fluorescence microscopy images (left) and fluorescence intensity profiles (right) of HUVECs treated with MSC-NVs or MSC-NV-N_3 (DiO; green). Before treatment, both MSC-NVs and MSC-NV-N_3 were reacted with DBCO-IL-10 (Alexa fluor 647; red) and purified. Scale bar: 50 μm.

Ac_4ManNAz concentrations (Fig. S2†), and we observed that 50 μM Ac_4ManNAz does not induce significant cytotoxic effects. Next, MSC-NVs and MSC-NV-N_3 were fabricated by serial extrusion. To confirm the stable exposure of the azide functional groups on MSC-NV-N_3 after fabrication, DBCO-Cy5 was incubated with NVs. Flow cytometry histogram and MFI analysis revealed that MSC-NV-N_3 bound DBCO-Cy5 with a 2.64-fold higher MFI than MSC-NVs (Fig. 2C), indicating effective preservation of azide moieties in fabricated NVs. Cryo-TEM imaging showed that MSC-NV-N_3 maintained a lipid bilayer structure with a spherical morphology (Fig. 2D), suggesting that metabolic engineering does not affect the exosome-like structure of fabricated NVs. Subsequently, prepared DBCO-PEG_4-IL-10 was conjugated to MSC-NV-N_3 to generate the final product, MSC-NV/IL-10. Following purification, the size and zeta potential of the NVs were measured. The mean diameter of MSC-NVs, MSC-NV-N_3, and MSC-NV/IL-10 was 139.03 ± 19.75, 148.03 ± 17.23, and 174.6 ± 5.71, respectively (Fig. 2E). The zeta potential of MSC-NVs, MSC-NV-N_3, and MSC-NV/IL-10 was −4.11 ± 0.71, −5.64 ± 0.7, and −7.89 ± 0.66, respectively (Fig. 2F). The observed changes in hydrodynamic size and zeta potential of MSC-NV/IL-10 support the successful conjugation of DBCO-PEG_4-IL-10 to MSC-NV-N_3. Additionally, NTA measurement showed that the fabricated NVs exhibit a uniform size distribution following the purification steps (Fig. S3†). The size distribution of NVs indicated that metabolic labeling did not alter the structural integrity. Next, DiO-labeled MSC-NVs and MSC-NV-N_3 were applied to HUVECs following conjugation with DBCO-Cy5 and subsequently observed with a fluorescence microscope (Fig. S4†). HUVECs treated with MSC-NV-N_3 exhibited significantly higher Cy5 fluorescence intensity (red) compared to MSC-NV-treated cells. Furthermore, fluorescence intensity profiles revealed a high level of co-localization between Cy5 and DiO signals in the MSC-NV-N_3 group. To verify the stable conjugation of IL-10 with MSC-NV-N_3, DBCO-IL-10 was fluorescently labeled with Alexa fluor 647 *via* maleimide chemistry. Alexa fluor 647-labeled DBCO-IL-10 was conjugated to DiO-stained MSC-NVs or MSC-NV-N_3 (MSC-NV/IL-10). Subsequent fluorescence microscope observation showed the co-localization of fluorescence signals from NVs and IL-10 in MSC-NV/IL-10 (Fig. 2G). Meanwhile, we did not observe clear fluorescence signals from IL-10 in MSC-NVs reacted with DBCO-IL-10, which is likely due to an absence of the N_3 moiety. Collectively, these results demonstrate that DBCO-tagged IL-10 was effectively conjugated to N_3-displaying NVs *via* click chemistry.

MSC-NV/IL-10 enhances the regenerative properties of fibroblast and endothelial cells

The angiogenic potential of MSC-NV/IL-10 was evaluated in L929 fibroblast cells and HUVECs. Proliferation and migration assays were carried out by incubating cells with various NVs in serum-free medium. A scratch assay was performed to assess the wound healing properties of L929 cells and HUVECs (Fig. 3A and B). The results revealed that MSC-NV/IL-10 exerted the most prominent enhancement in cell migration in both L929 and HUVECs up to 48 h post-treatment. Furthermore, a CCK-8 assay demonstrated that the MSC-NV/IL-10-treated group exhibited a 1.92-fold increase in L929 cell proliferation and a 2.06-fold increase in HUVEC proliferation compared to the control group (Fig. 3C). These findings indicate that MSC-NV/IL-10 more effectively promotes regenerative effects in endothelial and fibroblast cells compared to other groups. In addition, qRT-PCR analysis was carried out to compare the mRNA expression levels of angiogenic growth factors in L929 and HUVECs 48 h post-treatment (Fig. 3D). The results revealed that genes encoding angiogenic factors were significantly upregulated in groups treated with NVs, as compared to the control group. Particularly, HUVECs treated with MSC-NV/IL-10 exhibited the most prominent upregulation of HGF, FGF2, and Ang-1 expression levels.

Anti-apoptotic effects of MSC-NV/IL-10

We next evaluated the anti-apoptotic effect of MSC-NV/IL-10 in an H_2O_2-induced oxidative stress model in HUVECs. Cells exposed to various NVs were double-stained with Annexin V (FITC) and propidium iodide (PI), and the percentage of apoptotic cells was quantified by flow cytometry (Fig. 4A). H_2O_2 treatment significantly increased both Annexin V-positive and PI-positive populations, from 14.8% to 52.1% and 2.5% to 20.5%, respectively. Notably, MSC-NV/IL-10 treatment significantly reduced the percentages of Annexin V-positive cells (total apoptotic cells), Annexin V^+/PI^- (early apoptotic cells), and Annexin V^+/PI^+ (late apoptotic cells) relative to other groups. This flow cytometry analysis indicates that MSC-NV/IL-10 effectively inhibits the apoptosis in HUVECs under oxidative stress conditions. Additionally, qRT-PCR was performed to compare the relative mRNA expression of apoptosis-related genes, Bcl-2 and Bax (Fig. 4B). The results showed that the relative expression of the anti-apoptotic gene Bcl-2 was significantly upregulated, while the expression of the pro-apoptotic gene Bax was downregulated in the MSC-NV/IL-10-treated group. Collectively, these findings demonstrate the therapeutic potential of MSC-NV/IL-10 in the suppression of apoptosis under oxidative stress.

Effects of MSC-NV/IL-10 on macrophage polarization

To investigate the effects of MSC-NV/IL-10 on macrophage polarization, BMDMs were co-treated with LPS/IFN-γ and various NVs for 24 h. Macrophage phenotypes were characterized using F4/80 as a macrophage-specific marker. The expression of CD86, a representative marker of pro-inflammatory M1 macrophages, was evaluated by flow cytometry (Fig. 5A). The percentage of CD86-positive cells in the LPS/IFN-γ-treated group was 44.93 ± 1.39%, and the population decreased to 27.06 ± 3.70% in the MSC-NV/IL-10 treated group. There were no significant differences in the expression of CD206, a widely used marker for identifying M2 macrophages (Fig. S5†). Because treatment with LPS/IFN-γ also promotes the activation of the M2 marker, this result is possible due to an excess amount of stimulating factors, which hindered the observation of differences. Next, to compare the relative mRNA

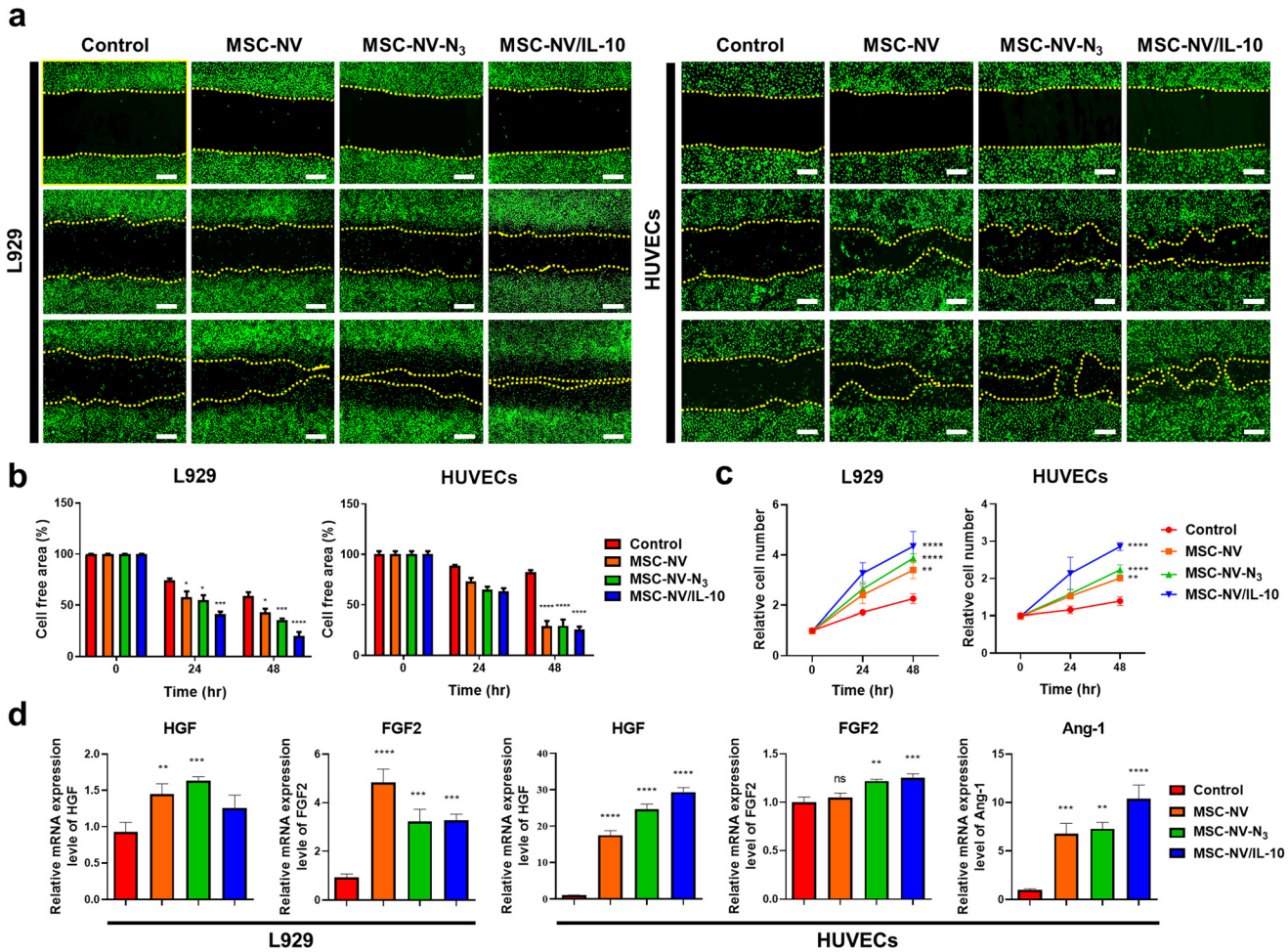

Fig. 3 MSC-NV/IL-10 shows enhanced regenerative effects in fibroblast and endothelial cells. (a) Scratch assay showing the wound healing properties of L929 cells and HUVECs after different treatments of NVs. Cells are stained with DiO (green). Scale bar: 500 μm. (b) Quantification of the cell-free area of L929 cells and HUVECs (n = 3). (c) Proliferative behavior of L929 and HUVECs measured until 48 h post-treatment (n = 3). (d) qRT-PCR analysis for the evaluation of mRNA expression of angiogenesis-related growth factors in L929 and HUVECs (n = 5). Treatment with PBS served as a control. Data are shown as mean ± SD with significance at *p < 0.05, **p < 0.01, ***p < 0.005, and ****p < 0.001.

expression of M1 and M2 markers in BMDMs, qRT-PCR was performed (Fig. 5B). The mRNA expression of M1 markers (IL-1β, TNF-α, and IL-6) was significantly downregulated, while the M2 macrophage-specific Arg-1 marker was predominantly upregulated following MSC-NV/IL-10 treatment. These *in vitro* results demonstrate that MSC-NV/IL-10 effectively attenuates pro-inflammatory responses in macrophages.

Induction of tolerogenic dendritic cells (tolDCs) by MSC-NV/IL-10

We next determined whether MSC-NV/IL-10 could induce activated BMDCs to become tolerogenic dendritic cells (tolDCs). Given that tolDCs typically exhibit low expression levels of surface costimulatory molecules (CD80, CD86, and CD40), which are typically upregulated during DC maturation.[35] Therefore, the expression of CD80, CD86, and CD40, which are markers for mature DCs (mDCs), was analyzed using flow cytometry following treatment with different NVs (Fig. 6A). To induce the maturation of immature DCs (imDCs) into mDCs, LPS was co-administered. Different groups of DCs were gated on CD11c expression, and the population of CD86, CD80, and CD40-positive cells was assessed and quantified (Fig. 6B). Compared to mDCs, MSC-NV/IL-10-treated DCs exhibited a marked reduction in these costimulatory markers, representing the semi-mature phenotype of tolDCs.

RNA-seq analysis of metabolically engineered MSCs

To explain the impact of metabolic engineering on the regenerative and immunomodulatory properties of MSCs, comprehensive RNA-seq analysis was carried out on both MSCs and Ac_4ManNAz-treated MSC-N_3. Density distribution curves of MSCs and MSC-N_3 exhibited a comparable overall shape (Fig. 7A), although MSCs displayed a slightly higher density in the low expression range, suggesting the potential downregulation of certain genes in response to Ac_4ManNAz treatment. To identify the number of differentially expressed genes (DEGs), a Venn diagram analysis was carried out (Fig. 7B). A Venn diagram revealed that 10 881 genes were commonly expressed

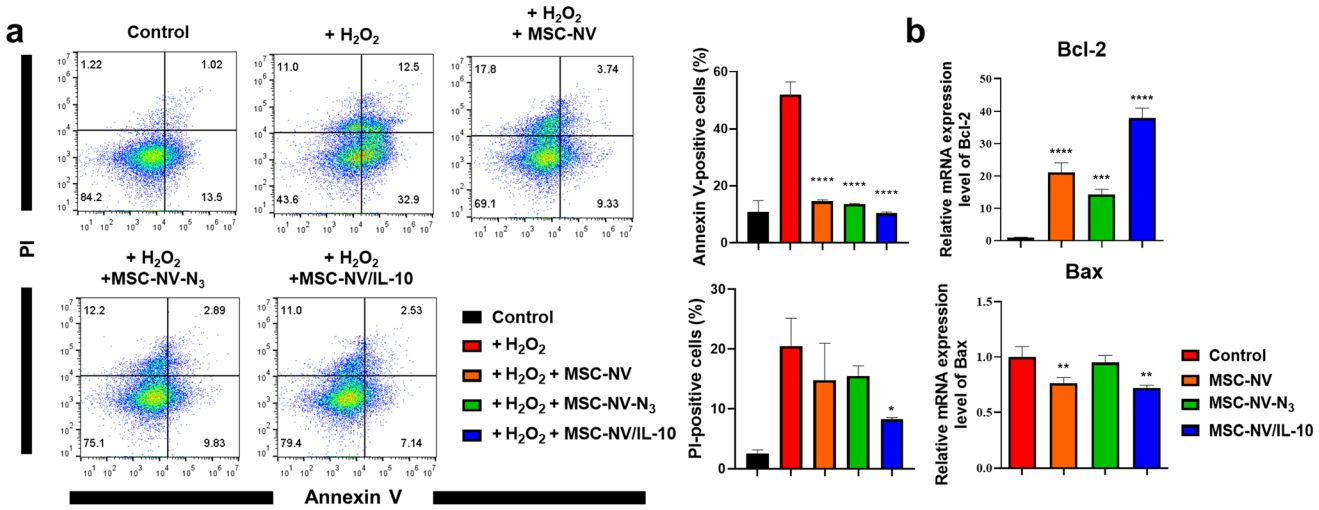

Fig. 4 Enhanced anti-apoptotic effects of MSC-NV/IL-10 in damaged endothelial cells. (a) Apoptotic behavior of HUVECs upon treatment with 1 mM H_2O_2 with co-treatment with MSC-NVs, MSC-NV-N_3, or MSC-NV/IL-10. HUVECs were double-stained with Annexin V-FITC and propidium iodide (PI) and determined using flow cytometry. Quantitative analysis of flow cytometry was also carried out (n = 3). *p versus* +H_2O_2 group. (b) qRT-PCR analysis to evaluate mRNA expression of anti-apoptotic Bcl-2 and pro-apoptotic Bax genes after treatment with different NVs (n = 5). Treatment with PBS served as a control. *p versus* the control group. *p < 0.05, **p < 0.01, ***p < 0.005, and ****p < 0.001.

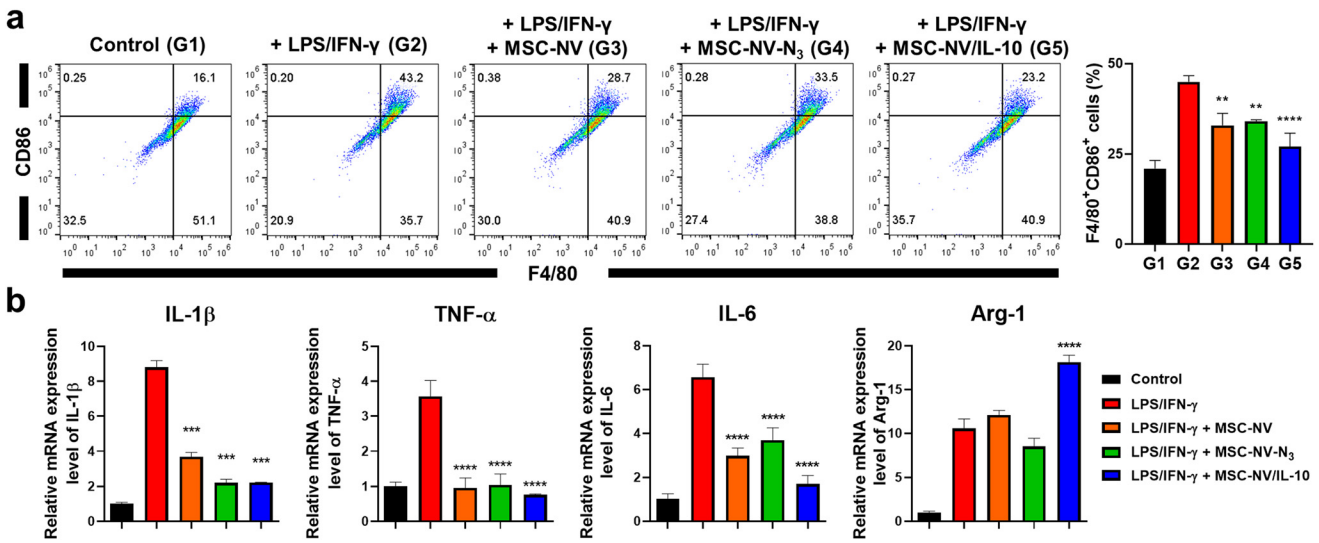

Fig. 5 MSC-NV/IL-10 effectively attenuates pro-inflammatory BMDMs and shows anti-inflammatory effects. (a) Flow cytometric plots showing the population of pro-inflammatory F4/80$^+$CD86$^+$ BMDMs upon treatment with various NVs in the presence of LPS and IFN-γ. Quantitative analysis of F4/80$^+$CD86$^+$ population was also carried out (n = 3). *p versus* G2. (b) qRT-PCR analysis of pro-inflammatory M1 markers (IL-1β, TNF-α, and IL-6) and anti-inflammatory M2 marker (Arg-1) in BMDMs treated with different NVs in the presence of LPS/IFN-γ (n = 3). *p versus* LPS/IFN-γ. Treatment with PBS served as a control. Data are shown as mean ± SD with significance at *p < 0.05, **p < 0.01, ***p < 0.005, and ****p < 0.001.

in both groups, indicating that fundamental cellular processes remain unaffected. A volcano plot was constructed to visualize DEGs between MSCs and MSC-N_3 (Fig. 7C). It is noteworthy that 186 genes were upregulated, while 274 genes were downregulated in response to Ac_4ManNAz treatment. However, statistical evaluation demonstrated that although most of the gene fold changes were minimal and did not reach significance thresholds. Therefore, in the volcano plot, 98.14% of genes exhibited non-significant expression in MSC-N_3. Gene ontology (GO) enrichment analysis demonstrated distinct functional patterns, though overall expression profiles remained largely unchanged (Fig. 7D). The functional analysis of the top 10 upregulated and downregulated genes was performed based on GO terms (Fig. 7E). Upregulated genes implicated functions in nuclear regulation, proteolysis, RNA binding, and energy metabolism, while downregulated genes play roles in intracellular organelles, DNA binding, and transmembrane signaling receptor activity. Although partial enrichment in immune

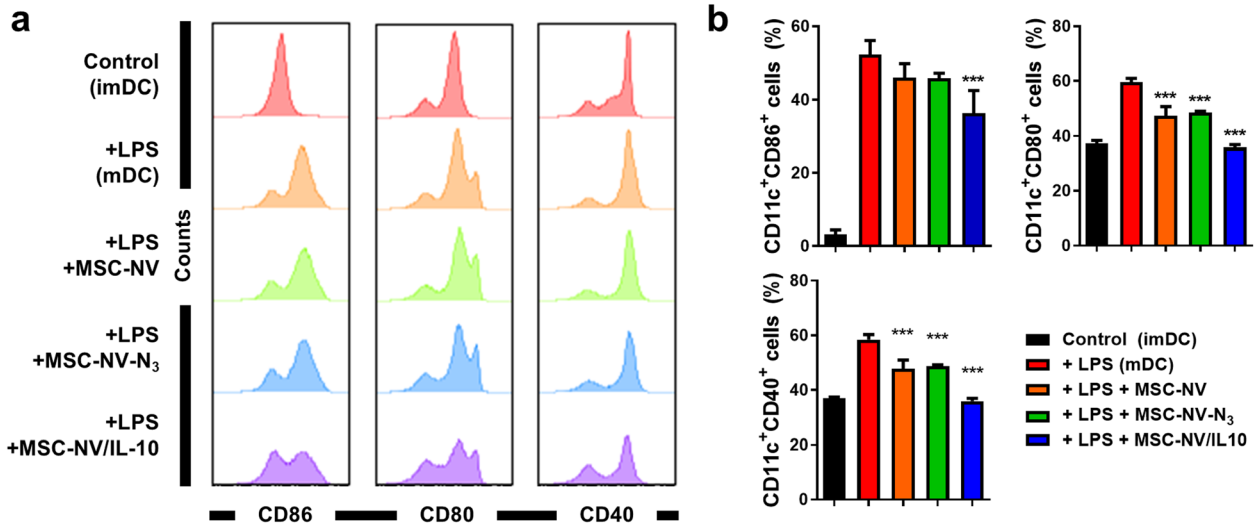

Fig. 6 MSC-NV/IL-10 induces tolerogenic dendritic cells (tolDCs). (a) Representative flow cytometric histograms showing the population of $CD86^+$, $CD80^+$, or $CD40^+$ BMDCs upon treatment with various NVs in the presence of LPS. BMDCs were gated by CD11c. (b) Quantitative analysis of $CD86^+$, $CD80^+$, or $CD40^+$ population in groups of BMDCs treated with different NVs in the presence of LPS in culture medium (n = 3). *p versus* to +LPS (mDC). Treatment with PBS served as a control. Data are shown as mean ± SD with significance at $^*p < 0.05$, $^{**}p < 0.01$, $^{***}p < 0.005$, and $^{****}p < 0.001$.

response and RNA splicing was observed, these changes were not statistically significant. Overall, the RNA-seq data suggest that Ac_4ManNAz treatment does not induce meaningful transcriptional alterations affecting the regenerative or immunomodulatory functions of MSCs.

Wound healing effect of MSC-NV/IL-10 in mouse skin injury model

To investigate the wound healing capacity of MSC-NV/IL-10 *in vivo*, full-thickness wound models were generated. Wound images were captured every three days over a nine-days period to monitor wound closure (Fig. 8A). Compared to the control and MSC-NV-treated groups, the MSC-NV/IL-10-treated group exhibited significantly accelerated wound healing (Fig. 8B). On day 9, the wound area was reduced to 1.6% of the initial size, while the control group and MSC-NV-treated group showed 28.8% and 17.5%, respectively. Histological analysis further showed enhanced tissue regeneration and re-epithelialization in MSC-NV/IL-10-treated group (Fig. 8C). The length of the wound was measured for quantitative assessment of wound healing, and the most prominent re-epithelialization was observed in MSC-NV/IL-10-treated mice. Next, immunostaining was performed to visualize the macrophage-specific F4/80, M1-specific iNOS, and M2-specific CD163 markers in injured site (Fig. 8D). Quantitative measurement of fluorescence showed that the expression of iNOS was significantly attenuated, whereas expressions of CD163 was higher than those of the other groups (Fig. 8E). In addition, resident DCs in skin tissue were assessed using DC-specific CD11c marker. Activation and maturation of DCs were evaluated by determining the expressions of CD80 and CD86 co-stimulatory molecules (Fig. 8F). We observed lowest staining scores of CD80 and CD86 in MSC-NV/IL-10-treated group (Fig. 8G), which is in accordance with aforementioned *in vitro* result showing the tolDC-inducing properties of MSC-NV/IL-10. These results collectively indicate that MSC-NV/IL-10 treatment reduces pro-inflammatory M1 macrophage while promoting tissue-regenerative M2 macrophages and tolDC at the wound site.

Discussion

The potential of MSC-derived EVs for disease diagnosis and tissue repair has been extensively investigated.[36,37] Previous studies have suggested that overexpression of IL-10 in MSCs or the encapsulation of IL-10 within MSC-EVs enhances neuroprotective and anti-inflammatory effects.[38,39] Moreover, co-treatment with MSC-EVs and IL-10 has been shown to improve IL-10 stability and facilitate targeted delivery to the injury sites, promoting remarkable M2 macrophage polarization.[23,40] However, conventional methods of IL-10 delivery present several challenges, including low efficiency, potential cytotoxicity, and inconsistent outcomes due to rapid degradation and difficulties in precise tissue targeting.[41,42] To overcome these limitations while preserving the inherent therapeutic characteristics of MSCs, we incorporated IL-10 into MSC-derived exosome-mimetic NVs *via* bio-orthogonal click chemistry. Ac_4ManNAz, a metabolic precursor for click chemistry, enables surface labeling of the cell membrane without interfering with internal cellular processes.[43] Consistent with this, our RNA-seq analysis confirmed that metabolic labeling did not induce significant genetic alterations in MSCs, although specific genes exhibited minor expression changes, these differences were not statistically significant.[44] These RNA-seq

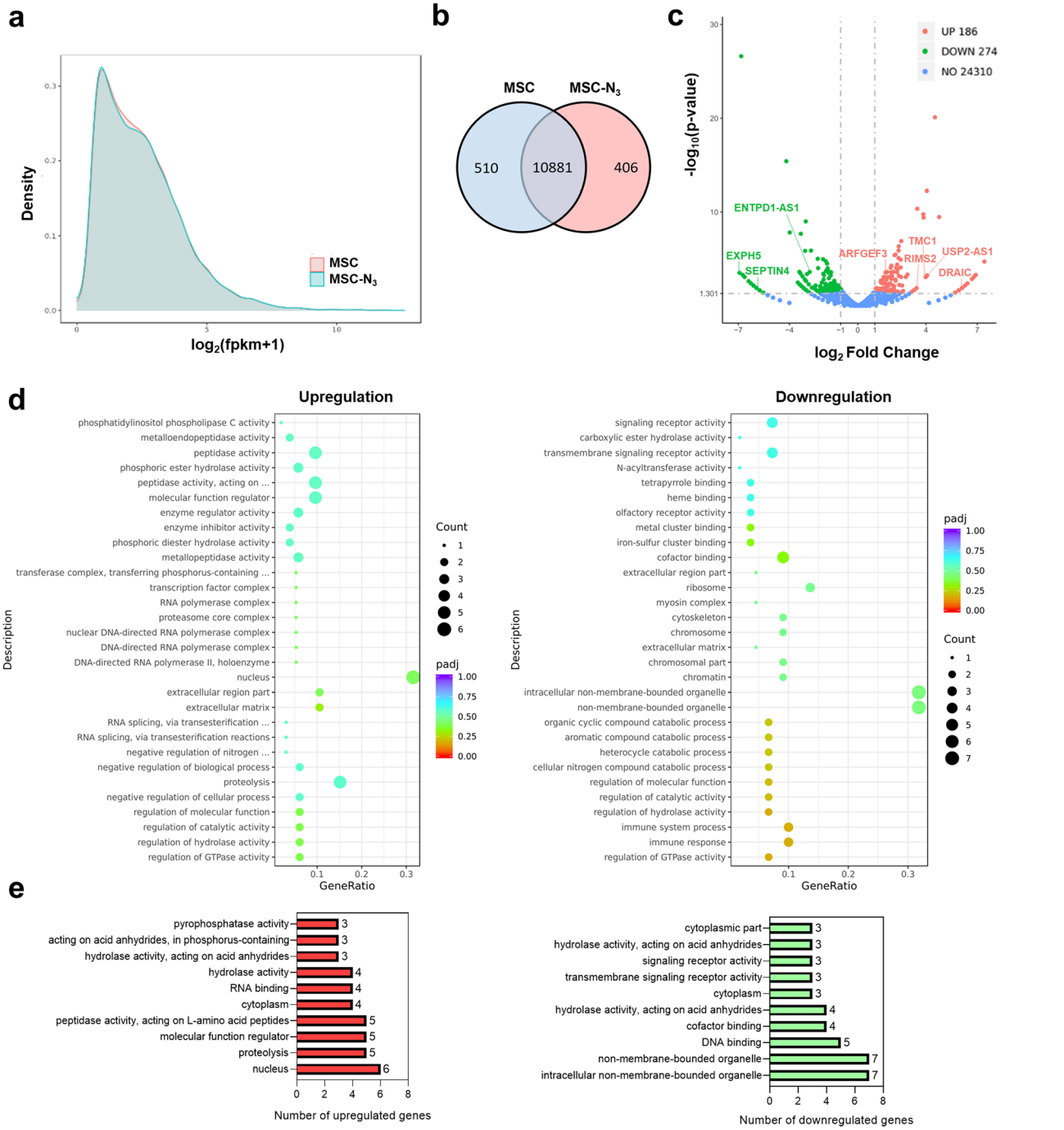

Fig. 7 RNA-seq analysis on MSCs and metabolically engineered MSC-N_3. Analysis of differentially expressed genes (DEGs) in MSCs and MSC-N_3. (a) Fragments per kilobase of transcript per million mapped reads (FPKM) density distribution of gene expression. (b) Venn diagrams of DEGs in MSCs and MSC-N_3. (c) Volcano plot showing the statistical significance of DEG data (adjusted *p*-value) *versus* magnitude of expression change (log_2 fold change) from the comparison of MSCs and MSC-N_3. (d) Gene sets significantly enriched or down-regulated in MSC-N_3 using Gene Ontology (GO) biological processes. (e) The functional analysis of the top 10 upregulated and downregulated genes.

results emphasize the safety and non-disruptive characteristics of metabolic engineering, particularly when compared with other MSC-stimulating conditions, such as 3D culture, which are known to induce genetic modifications.[45,46] The bio-orthogonal reaction thus provides a highly specific and controlled labeling approach, without interfering with critical cellular processes, including wound healing and anti-inflammatory modulation of MSCs.[47,48] MSC-NVs were engineered to express azide (N_3) groups on their surface, while IL-10 was modified with DBCO, enabling highly specific conjugation *via*

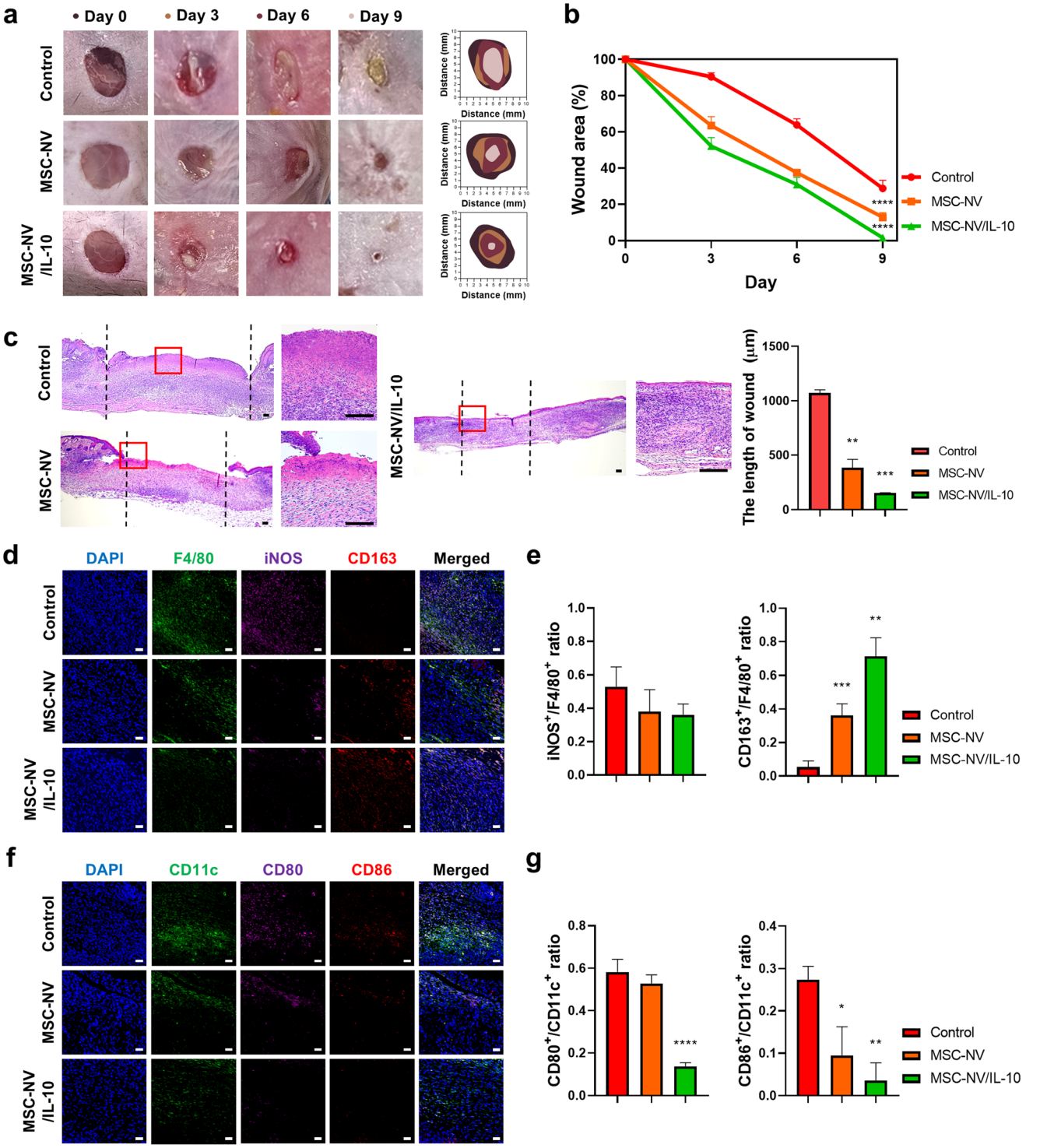

Fig. 8 Wound healing effect of MSC-NV/IL-10 in mouse skin injury. (a) Digital images of the wound site at 3, 6, and 9 days after treatment with PBS (control), MSC-NVs, or MSC-NV/IL-10. (b) Quantitative measurement of the wound areas. (c) H&E-stained skin tissues (left) and quantification of the wound length (right). Wounds are indicated with dashed lines. Scale bar: 100 μm. (d) Immunofluorescence staining of the wound site for F4/80, iNOS, and CD163 at day 6. (e) Quantification of $iNOS^+$ and $CD163^+$ relative to $F4/80^+$ cells in immunofluorescence images from the wound site. (f) Immunofluorescence staining of the wound site for CD11c, CD80, and CD86 at day 6. (g) Quantification of $CD80^+$ and $CD86^+$ relative to $CD11c^+$ cells in immunofluorescence images from the wound site. Scale bar: 100 μm. Data are shown as mean ± SD with significance at $*p < 0.05$, $**p < 0.01$, $***p < 0.005$, and $****p < 0.001$.

click chemistry. Owing to the lipid bilayer structure of MSC-NVs, IL-10 cannot spontaneously diffuse across the membrane due to the physical separation between the inner and outer membranes, making intravesicular localization highly unlikely. Accordingly, fluorescence imaging of MSC-NV/IL-10 demonstrates that IL-10 is exclusively localized on the external surface of the vesicles.

Compared with naturally secreted exosomes, MSC-NV/IL-10 offers significant advantages in terms of large-scale production, consistent quality, and targeted delivery, while maintaining stability.[49,50] It is well established that intravenously administered MSC-EVs tend to accumulate in the liver due to uptake by the mononuclear phagocyte system.[51] Similarly, IL-10 binds to IL-10 receptor (IL-10R)-expressing immune cells in inflamed tissues or specific tumor cells.[52] However, its rapid clearance remains a major limitation. While various nanocarriers have been developed for the precise and efficient delivery of proteins and cytokines,[53,54] our MSC-NV/IL10 conjugation approach enhances the therapeutic potential of protein-based treatments and improves immunotherapy.

Consistent with recent comprehensive studies,[55,56] our findings support the regenerative and immunomodulatory potential of MSC-NVs in skin wound healing, while IL-10 augments both angiogenesis and immune modulation. Although IL-10 is traditionally recognized for its immunosuppressive properties, it also promotes angiogenesis by upregulating the expression of angiogenesis-related factors such as vascular endothelial growth factor (VEGF), fibroblast growth factor (FGF), and angiopoietin-1 (Ang-1)[57–59] and facilitating scar-free healing by modulating immune response.[60] Mechanistically, IL-10 enhances the immunomodulatory function by binding to its receptor on immune cells, subsequently activating the JAK-STAT3 signaling pathway.[61,62] This signaling cascade suppresses pro-inflammatory NF-κB activity and upregulation of anti-inflammatory mediators, which promote M2 macrophage polarization.[63] While MSC-NVs exert immunoregulatory potential, the functionalization with IL-10 provides a more robust polarization toward the M2 phenotype. In addition, IL-10 leads to enhanced secretion of pro-angiogenic factors such as VEGF and matrix metalloproteinases (MMPs), supporting extracellular matrix remodeling and endothelial cell migration.[58] Notably, IL-10 treatment during the early inflammatory phase did not interfere with tissue regeneration. Instead, it accelerated wound closure and promoted a shift toward a pro-regenerative immune response.[64,65] Given that all NV groups were treated with equal concentrations, the enhanced effects observed in the MSC-NV/IL-10 group can be attributed to the functional properties of IL-10 or synergistically interact with intrinsic MSC-NV components. Consequently, MSC-NV/IL-10 exhibited a substantial effect on cell migration and proliferation, as further supported by our qPCR results showing elevated mRNA expression levels of several angiogenesis. Nonetheless, despite the pro-angiogenic effects of IL-10, its primary role remains immune modulation.[23] Indeed, some angiogenesis-related matrices in the MSC-NV/IL-10 group were comparable to those observed in non-engineered MSC-NVs. In contrast, immunomodulatory assays revealed that MSC-NV/IL-10 exerted significantly stronger anti-inflammatory effects and induced a higher proportion of tolDC compared to MSC-NVs without IL-10 functionalization.

In addition to their angiogenic and immunomodulatory properties, MSC-NVs exert protective effects by modulating oxidative stress, suppressing pro-apoptotic signaling, and enhancing cell survival pathways. MSC-NVs transport a diverse range of miRNAs, lncRNAs, and circRNAs, that regulate the expression of apoptosis-related genes such as caspase-8/-9/-3/-7.[49] Moreover, IL-10 has been reported to enhance cell survival under oxidative stress by activating ERK1/2 signaling through tyrosine phosphorylation.[66] Collectively, treatment with MSC-NV/IL-10 significantly enhanced the anti-apoptotic effects in HUVECs under oxidative stress. Furthermore, our *in vivo* investigations confirmed the therapeutic efficacy of MSC-NV/IL-10. In the wound model, groups treated with MSC-NV/IL-10 exhibited markedly accelerated wound closure. Additionally, immunofluorescence staining demonstrated a significant reduction in the infiltration of pro-inflammatory M1 macrophages, with an increased presence of anti-inflammatory M2 macrophages and tolDCs at the wound site. These findings suggest that the conjugation of MSC-NVs with IL-10 provides complementary therapeutic effects by integrating regenerative and immunomodulatory functions. Importantly, these therapeutic effects were suggested through topical administration of MSC-NV/IL-10 directly to the wound site. Topical delivery enables localized absorption of MSC-NV/IL-10 through the damaged skin barrier, enhancing targeted activity while minimizing systemic distribution. Previous studies have demonstrated that topically applied exosomes and EVs exhibit local retention and bioactivity within the wound tissue. Furthermore, topically delivered EVs were rapidly internalized into wound tissue without significant off-target effects.[67,68] This localized approach enables to maximization of therapeutic efficacy while reducing potential systemic side effects. Given the inherent advantages of MSC-derived EVs,[69] our suggested MSC-NV/IL-10 represents a promising strategy for applications in regenerative medicine and immunotherapy.

Conclusion

In this study, we demonstrated the effective labeling of MSC-NVs with the immunomodulatory cytokine IL-10 *via* bioorthogonal click chemistry. Metabolic glycoengineering of MSCs resulted in the expression of an azide functional group on the plasma membrane of MSCs, and these moieties were stably transferred to fabricated NVs. The azide-displaying NVs were efficiently conjugated with DBCO-tagged IL-10 *via* click chemistry. *In vitro*, the as-synthesized MSC-NV/IL-10 exerted outstanding regenerative effects in fibroblast and endothelial cells and effectively promoted anti-inflammatory responses in both macrophages and DCs. Furthermore, RNA-seq of MSCs and MSC-N_3 revealed that metabolic engineering does not alter the cellular pathways involved in the regenerative or

immunomodulatory role of MSCs. Importantly, *in vivo* investigations demonstrated accelerated wound healing, enhanced tissue regeneration, and reduced inflammatory responses in mouse wound models treated with MSC-NV/IL-10. These results collectively emphasize the feasibility of metabolic engineering, particularly in MSC- or MSC-NV-based tissue engineering and regenerative medicine.

Conflicts of interest

There are no conflicts of interest to declare.

Ethical statement

All animal experimental procedures were performed according to the guidelines and with the approval of the Institutional Animal Care and Use Committee (IACUC) of The Catholic University of Korea (IACUC number: CUK-IACUC-2023-010).

Data availability

The authors declare that all data supporting the results of this study are available within the paper and its additional file.

Acknowledgements

This work was supported by the National Research Foundation of Korea (NRF) grant funded by the Korean government (MSIT) (RS-2022-NR071672) and by a grant of the Korea Health Technology R&D Project through the Korea Health Industry Development Institute (KHIDI), funded by the Ministry of Health & Welfare, Republic of Korea (RS-2023-KH135936).

References

1 T. Zhang, Y. W. Lee, Y. F. Rui, T. Y. Cheng, X. H. Jiang and G. Li, *Stem Cell Res. Ther.*, 2013, **4**, 1–15.
2 M. Kou, L. Huang, J. Yang, Z. Chiang, S. Chen, J. Liu, L. Guo, X. Zhang, X. Zhou and X. Xu, *Cell Death Dis.*, 2022, **13**, 580.
3 E. Eggenhofer, V. Benseler, A. Kroemer, F. Popp, E. Geissler, H. Schlitt, C. Baan, M. Dahlke and M. Hoogduijn, *Front. Immunol.*, 2012, **3**, 297.
4 A. Gowen, F. Shahjin, S. Chand, K. E. Odegaard and S. V. Yelamanchili, *Front. Cell Dev. Biol.*, 2020, **8**, 149.
5 Y. Sun, F. Sun, W. Xu and H. Qian, *Tissue Eng. Regener. Med.*, 2023, **20**, 157–175.
6 M. Mastri, H. Lin and T. Lee, *World J. Stem Cells*, 2014, **6**, 82–93.
7 Q. Li, Z. Wang, N. Shi, Y. Qi, W. Yao, J. Yu and Y. Lu, *Smart Med.*, 2023, **2**, e20230030.
8 H. Y. Kim and S. H. Bhang, *Materials*, 2021, **14**, 1078.
9 J.-R. Lee, B.-W. Park, J. Kim, Y. W. Choo, H. Y. Kim, J.-K. Yoon, H. Kim, J.-W. Hwang, M. Kang, S. P. Kwon, S. Y. Song, I. O. Ko, J.-A. Park, K. Ban, T. Hyeon, H.-J. Park and B.-S. Kim, *Sci. Adv.*, 2020, **6**, eaaz0952.
10 K.-S. Park, K. Svennerholm, G. V. Shelke, E. Bandeira, C. Lässer, S. C. Jang, R. Chandode, I. Gribonika and J. Lötvall, *Stem Cell Res. Ther.*, 2019, **10**, 231.
11 T. Xia, S. Fu, R. Yang, K. Yang, W. Lei, Y. Yang, Q. Zhang, Y. Zhao, J. Yu and L. Yu, *J. Inflammation*, 2023, **20**, 33.
12 K.-S. Park, E. Bandeira, G. V. Shelke, C. Lässer and J. Lötvall, *Stem Cell Res. Ther.*, 2019, **10**, 1–15.
13 J. P. Armstrong, M. N. Holme and M. M. Stevens, *ACS Nano*, 2017, **11**, 69–83.
14 D. G. You, G. T. Lim, S. Kwon, W. Um, B. H. Oh, S. H. Song, J. Lee, D.-G. Jo, Y. W. Cho and J. H. Park, *Sci. Adv.*, 2021, **7**, eabe0083.
15 J. Tang, X. Wang, X. Lin and C. Wu, *Cell Death Discovery*, 2024, **10**, 212.
16 M. Nakajima, C. Nito, K. Sowa, S. Suda, Y. Nishiyama, A. Nakamura-Takahashi, Y. Nitahara-Kasahara, K. Imagawa, T. Hirato and M. Ueda, *Mol. Ther. – Methods Clin. Dev.*, 2017, **6**, 102–111.
17 M. Saraiva, P. Vieira and A. O'Garra, *J. Exp. Med.*, 2019, **217**(1), e20190418.
18 Y. Zhang, X. Zhang, H. Zhang, P. Song, W. Pan, P. Xu, G. Wang, P. Hu, Z. Wang and K. Huang, *Front. Immunol.*, 2022, **12**, 811164.
19 T. Bu, Z. Li, Y. Hou, W. Sun, R. Zhang, L. Zhao, M. Wei, G. Yang and L. Yuan, *Theranostics*, 2021, **11**, 9988.
20 R. L. Lopes, T. J. Borges, R. F. Zanin and C. Bonorino, *Cytokine*, 2016, **85**, 123–129.
21 E. B. Lurier, D. Dalton, W. Dampier, P. Raman, S. Nassiri, N. M. Ferraro, R. Rajagopalan, M. Sarmady and K. L. Spiller, *Immunobiology*, 2017, **222**, 847–856.
22 Y. K. Kim, S. E. Kim, H. C. Park, J. H. Hwang and H. T. Lee, *Biochem. Biophys. Rep.*, 2020, **24**, 100857.
23 M. A. Boks, J. R. Kager-Groenland, M. S. Haasjes, J. J. Zwaginga, S. M. van Ham and A. ten Brinke, *Clin. Immunol.*, 2012, **142**, 332–342.
24 A. Cifuentes-Rius, A. Desai, D. Yuen, A. P. R. Johnston and N. H. Voelcker, *Nat. Nanotechnol.*, 2021, **16**, 37–46.
25 X. Zhang, J. Liu, L. Wu and X. Hu, *eLife*, 2020, **9**, e55676.
26 F. Minshawi, S. Lanvermann, E. McKenzie, R. Jeffery, K. Couper, S. Papoutsopoulou, A. Roers and W. Muller, *Front. Immunol.*, 2020, **11**, 1794.
27 C. Wang, D. Lv, X. Zhang, Z.-A. Ni, X. Sun and C. Zhu, *DNA Cell Biol.*, 2018, **37**, 53–61.
28 M. Gai, J. Simon, I. Lieberwirth, V. Mailänder, S. Morsbach and K. Landfester, *Polym. Chem.*, 2020, **11**, 527–540.
29 H. Wang and D. J. Mooney, *Nat. Chem.*, 2020, **12**, 1102–1114.
30 A. Mongis, F. Piller and V. Piller, *Bioconjugate Chem.*, 2017, **28**, 1151–1165.
31 H. Wang, M. Gauthier, J. R. Kelly, R. J. Miller, M. Xu, W. D. O'Brien Jr and J. Cheng, *Angew. Chem., Int. Ed.*, 2016, **55**, 5452–5456.

32 M. S. Chowdhury, W. Zheng, S. Kumari, J. Heyman, X. Zhang, P. Dey, D. A. Weitz and R. Haag, *Nat. Commun.*, 2019, **10**, 4546.
33 H. Ruan, Y. Li, C. Wang, Y. Jiang, Y. Han, Y. Li, D. Zheng, J. Ye, G. Chen and G.-Y. Yang, *Acta Pharm. Sin. B*, 2023, **13**, 2202–2218.
34 S. Rayamajhi and S. Aryal, *J. Mater. Chem. B*, 2020, **8**, 4552–4569.
35 M. Shahir, S. Mahmoud Hashemi, A. Asadirad, M. Varahram, M. Kazempour-Dizaji, G. Folkerts, J. Garssen, I. Adcock and E. Mortaz, *J. Cell. Physiol.*, 2020, **235**, 7043–7055.
36 J.-Y. Ding, M.-J. Chen, L.-F. Wu, G.-F. Shu, S.-J. Fang, Z.-Y. Li, X.-R. Chu, X.-K. Li, Z.-G. Wang and J.-S. Ji, *Mil. Med. Res.*, 2023, **10**, 36.
37 A. Casado-Díaz, J. M. Quesada-Gómez and G. Dorado, *Front. Bioeng. Biotechnol.*, 2020, **8**, 146.
38 M. Shao, D. Wang, Y. Zhou, K. Du and W. Liu, *Int. Immunopharmacol.*, 2020, **81**, 106212.
39 A. I. Nykänen, A. Mariscal, A. Duong, C. Estrada, A. Ali, O. Hough, A. Sage, B. T. Chao, M. Chen and H. Gokhale, *Mol. Ther. – Methods Clin. Dev.*, 2021, **23**, 184–197.
40 C. Gorby, J. Sotolongo Bellón, S. Wilmes, W. Warda, E. Pohler, P. K. Fyfe, A. Cozzani, C. Ferrand, M. R. Walter and S. Mitra, *Sci. Signaling*, 2020, **13**, eabc0653.
41 A. L. Ali, N. P. Nailwal and G. M. Doshi, *Endocr., Metab. Immune Disord.:Drug Targets*, 2022, **22**, 371–382.
42 Y. Nitahara-Kasahara, M. Kuraoka, Y. Oda, H. Hayashita-Kinoh, S. I. Takeda and T. Okada, *Stem Cell Res. Ther.*, 2021, **12**, 1–15.
43 Y. Wang and Q. Hu, *Adv. NanoBiomed Res.*, 2023, **3**, 2200128.
44 H. Wang, Y. Bo, Y. Liu, M. Xu, K. Cai, R. Wang and J. Cheng, *Biomaterials*, 2019, **218**, 119305.
45 R. Lu, K. Zheng, Y. Zhou, W. Wang, Y. Zhang, Y. Chen, M. Mo, X. Li, Y. Dong and J. Xie, *Iscience*, 2024, **27**, 110811.
46 B. Wang, W. Liu, J. J. Li, S. Chai, D. Xing, H. Yu, Y. Zhang, W. Yan, Z. Xu and B. Zhao, *Bioact. Mater.*, 2022, **7**, 478–490.
47 X. Hou, C. Ke and J. F. Stoddart, *Chem. Soc. Rev.*, 2016, **45**, 3766–3780.
48 H. Mirzaei, A. Sahebkar, L. S. Sichani, A. Moridikia, S. Nazari, J. Sadri Nahand, H. Salehi, J. Stenvang, A. Masoudifar and H. R. Mirzaei, *J. Cell. Physiol.*, 2018, **233**, 2815–2823.
49 L. Pang, H. Jin, Z. Lu, F. Xie, H. Shen, X. Li, X. Zhang, X. Jiang, L. Wu and M. Zhang, *Adv. Healthcare Mater.*, 2023, **12**, 2300315.
50 W. Jo, J. Kim, J. Yoon, D. Jeong, S. Cho, H. Jeong, Y. Yoon, S. Kim, Y. Gho and J. Park, *Nanoscale*, 2014, **6**, 12056–12064.
51 S. Wen, M. Dooner, E. Papa, M. Del Tatto, M. Pereira, T. Borgovan, Y. Cheng, L. Goldberg, O. Liang and G. Camussi, *Int. J. Mol. Sci.*, 2019, **20**, 5468.
52 Y. Fan, C. Wang, W. Dai, Y. Zhou, G. Lu, W. Li, L. Li and T. Lin, *ACS Appl. Mater. Interfaces*, 2024, **16**, 38979–38988.
53 S. Han and J. Wu, *ACS Appl. Mater. Interfaces*, 2022, **14**, 55944–55956.
54 T.-T. Tang, B. Wang, M. Wu, Z.-L. Li, Y. Feng, J.-Y. Cao, D. Yin, H. Liu, R.-N. Tang and S. D. Crowley, *Sci. Adv.*, 2020, **6**, eaaz0748.
55 I. Aydemir, Ş. Öztürk, P. K. Sönmez and M.İ Tuğlu, *Anatomy*, 2016, **10**, 228–234.
56 D. G. Phinney and M. F. Pittenger, *Stem Cells*, 2017, **35**, 851–858.
57 D. S. Dace, A. A. Khan, J. Kelly and R. S. Apte, *PLoS One*, 2008, **3**, e3381.
58 J. L. Suen, Y. Chang, Y. S. Shiu, C. Y. Hsu, P. Sharma, C. C. Chiu, Y. J. Chen, T. C. Hour and E. M. Tsai, *J. Pathol.*, 2019, **249**, 485–497.
59 R. Nakamura, A. Sene, A. Santeford, A. Gdoura, S. Kubota, N. Zapata and R. S. Apte, *Nat. Commun.*, 2015, **6**, 7847.
60 L. M. Wise, G. S. Stuart, N. C. Jones, S. B. Fleming and A. A. Mercer, *J. Clin. Med.*, 2020, **9**, 1085.
61 M. Saraiva and A. O'garra, *Nat. Rev. Immunol.*, 2010, **10**, 170–181.
62 M. Fioranelli and M. G. Roccia, *J. Integr. Cardiol.*, 2014, **1**, 2–6.
63 W. Ouyang, S. Rutz, N. K. Crellin, P. A. Valdez and S. G. Hymowitz, *Annu. Rev. Immunol.*, 2011, **29**, 71–109.
64 T. Lucas, A. Waisman, R. Ranjan, J. Roes, T. Krieg, W. Müller, A. Roers and S. A. Eming, *J. Immunol.*, 2010, **184**, 3964–3977.
65 W. H. Peranteau, L. Zhang, N. Muvarak, A. T. Badillo, A. Radu, P. W. Zoltick and K. W. Liechty, *J. Invest. Dermatol.*, 2008, **128**, 1852–1860.
66 T. John, R. Müller, A. Oberholzer, H. Zreiqat, B. Kohl, W. Ertel, A. Hostmann, S. Tschoeke and G. Schulze-Tanzil, *Cytokine*, 2007, **40**, 226–234.
67 L. Li, Y. Wang, Y. Xu, J. Xu, Y. Zhao, Z. Cheng, Y. Fang, Y. Miao and X. Zhang, *J. Controlled Release*, 2024, **371**, 298–312.
68 H.-H. Hsu, A. Y. L. Wang, C. Y. Y. Loh, A. A. Pai and H.-K. Kao, *Pharmaceutics*, 2022, **14**, 1206.
69 V. E. Getova, E. Orozco-García, S. Palmers, G. Krenning, R. Narvaez-Sanchez and M. C. Harmsen, *Tissue Eng. Regener. Med.*, 2024, **21**, 881–895.